

**CFBDSIR J1458+1013B:
A Very Cold ($>T10$) Brown Dwarf in a Binary System^{1,2,3}**

Michael C. Liu,⁴ Philippe Delorme,⁵ Trent J. Dupuy,^{6,7} Brendan P. Bowler,⁴
Loic Albert,⁸ Etienne Artigau,⁹ Celine Reyl  ,¹⁰ Thierry Forveille,⁵ Xavier Delfosse⁵

ABSTRACT

We have identified CFBDSIR J1458+1013 as a $0.11''$ (2.6 AU) physical binary using Keck laser guide star adaptive optics imaging and have measured a distance of 23.1 ± 2.4 pc to the system based on near-IR parallax data from CFHT. The integrated-light near-IR spectrum indicates a spectral type of T9.5, and model atmospheres suggest a slightly higher temperature and surface gravity than the T10 dwarf UGPS J0722–05. Thus, CFBDSIR J1458+1013AB is the coolest brown dwarf binary found to date. Its secondary component has an absolute H -band magnitude that is 1.9 ± 0.3 mag fainter than UGPS J0722–05, giving an inferred spectral type of $>T10$. The secondary’s bolometric luminosity of $\sim 2 \times 10^{-7} L_{\odot}$ makes it the least luminous known brown dwarf by

¹Some of the data presented herein were obtained at the W.M. Keck Observatory, which is operated as a scientific partnership among the California Institute of Technology, the University of California, and the National Aeronautics and Space Administration. The Observatory was made possible by the generous financial support of the W.M. Keck Foundation.

²Based on observations made with ESO Telescopes at the Paranal Observatory under programme 085.C-0805(A).

³Based on observations obtained with WIRC  , a joint project of CFHT, Taiwan, Korea, Canada, France, and the Canada-France-Hawaii Telescope (CFHT) which is operated by the National Research Council (NRC) of Canada, the Institut National des Sciences de l’Univers of the Centre National de la Recherche Scientifique of France, and the University of Hawaii.

⁴Institute for Astronomy, University of Hawai’i, 2680 Woodlawn Drive, Honolulu, HI 96822, USA; mliu@ifa.hawaii.edu.

⁵UJF-Grenoble 1 / CNRS-INSU, Institut de Plan  tologie et d’Astrophysique de Grenoble (IPAG) UMR 5274, Grenoble F-38041, France.

⁶Harvard-Smithsonian Center for Astrophysics, 60 Garden Street, Cambridge, MA 02138

⁷Hubble Fellow

⁸Canada-France-Hawaii Telescope Corporation, 65-1238 Mamalahoa Highway, Kamuela, HI 96743, USA

⁹D  partement de Physique and Observatoire du Mont M  gantic, Universit   de Montr  al, C.P. 6128, Succ. Centre-Ville, Montr  al, QC H3C 3J7, Canada.

¹⁰Observatoire de Besan  on, Universit   de Franche-Comt  , Institut Utinam, UMR CNRS 6213, BP 1615, 25010 Besan  on Cedex, France.

a factor of 4–5. By comparing to evolutionary models and T9–T10 objects, we estimate a temperature of 370 ± 40 K and a mass of 6–15 M_{Jup} for CFBDSIR J1458+1013B. At such extremes, atmospheric models predict the onset of novel photospheric processes, namely the appearance of water clouds and the removal of strong alkali lines, but their impact on the emergent spectrum is highly uncertain. Our photometry shows that strong CH_4 absorption persists at H -band; the $J - K$ color is bluer than the latest known T dwarfs but not as blue as predicted by current models; and the $J - H$ color delineates a possible inflection in the blueward trend for the latest T dwarfs. Given its low luminosity, atypical colors and cold temperature, CFBDSIR J1458+1013B is a promising candidate for the hypothesized Y spectral class. However, regardless of its ultimate classification, CFBDSIR J1458+1013AB provides a new benchmark for measuring the properties of brown dwarfs and gas-giant planets, testing substellar models, and constraining the low-mass limit for star formation.

Subject headings: binaries: general, close — stars: brown dwarfs — infrared: stars — techniques: high angular resolution

1. Introduction

Over the last 15 years, stellar and exoplanetary studies have been propelled through the study of brown dwarfs. Residing at the extremes of low mass, luminosity and temperature, brown dwarfs serve as laboratories for understanding gas-giant extrasolar planets as well as the faint end of the star formation process. The coolest known brown dwarfs, the T dwarfs, have temperatures (≈ 600 – 1400 K), bolometric luminosities ($\approx 10^{-4}$ to 10^{-6} L_{\odot}), molecule-dominated (H_2O and CH_4) IR spectra, and atmospheric processes (e.g., non-equilibrium chemistry) that are more akin to Jupiter than any star. This physical similarity drives the ongoing search for even more extreme objects, to close the gap of ≈ 400 K in temperature and factor of ≈ 1000 in L_{bol} between the coolest T dwarfs and the planet Jupiter. Along the way, one question to be answered is whether such new discoveries will have sufficiently distinct spectra to invoke the proposed “Y” spectral type (Kirkpatrick et al. 1999).

A well-established strategy for finding the coolest objects is to search for them as companions to other objects. This approach has been quite successful: the first L and T dwarfs were found as companions around hotter objects, GD 165B (Becklin & Zuckerman 1988) and Gl 229B (Nakajima et al. 1995), respectively. To date, some of the coolest T dwarfs are found as companions to stars: Gl 570 D (T7.5; Burgasser et al. 2000), HD 3651 B (T7.5; Mugrauer et al. 2006; Luhman et al. 2007), ULAS J1416+13 B (T7.5; Scholz 2010a; Burningham et al. 2010), GJ 758B (\approx T8–T9; Thalmann et al. 2009; Janson et al. 2011) Wolf 940B (T8.5; Burningham et al. 2009), and Ross 458C (T8.5; Goldman et al. 2010; Scholz 2010b).

Field L and T dwarfs themselves have long been recognized as promising search targets for even

cooler objects. To date, six secondary components later than T5 have been identified in binaries (see compilation in Liu et al. 2010), one of which has a short enough orbital period to yield a dynamical mass, the T5.0+T5.5 substellar binary 2MASS J1534–2952AB (Liu et al. 2008).¹ In addition, discovery of ultracool objects in binaries opens the door to direct mass measurements through astrometric and spectroscopic monitoring of their orbits.

As part of an ongoing program to study the multiplicity and physical properties of brown dwarfs using laser guide star adaptive optics (LGS AO), we present here the discovery of the binarity of CFBDSIR J1458+1013. This object was identified in deep z and J -band data by Delorme et al. (2010) and assigned a preliminary spectral type of T8.5 based on its H -band spectrum. We have scrutinized this object using a combination of high resolution imaging, near-IR astrometry, and near-IR spectroscopy. These data indicate an integrated-light spectral type of T9.5, which is later than all known field objects except the T10 dwarf UGPS J0722–05 (Lucas et al. 2010). The secondary component of CFBDSIR J1458+1013AB is ≈ 1.5 –2 mag fainter in absolute magnitude and ≈ 150 K cooler in temperature than any known brown dwarf, making it a promising candidate for the first member of the Y spectral class.

2. Observations

2.1. Keck LGS AO Imaging and Photometry

We imaged CFBDSIR J1458+1013 on UT 22 May 2010 and 08 July 2010 using the sodium LGS AO system of the 10-meter Keck II Telescope on Mauna Kea, Hawaii (Wizinowich et al. 2006; van Dam et al. 2006). We used the facility IR camera NIRC2 with its narrow field-of-view camera, which produces a $10.2'' \times 10.2''$ field of view. Conditions were photometric for both runs with excellent seeing: 0.5–0.6'' and 0.3–0.5'' FWHM in May and July, respectively, as measured by a differential image motion monitor located at the nearby Canada-France-Hawaii Telescope. The LGS provided the wavefront reference source for AO correction, with the tip-tilt motion measured contemporaneously from the $R = 15.5$ mag field star USNO-B1.0 1002–0236935 (Monet et al. 2003) located 55'' away from CFBDSIR J1458+1013. The LGS brightness, as measured by the flux incident on the AO wavefront sensor, was equivalent to a $V \approx 9.6$ and 10.3 mag star in May and July, respectively.

At each epoch, we obtained a series of dithered images by offsetting the telescope by a few arcseconds between each 1–2 images. The sodium laser beam was pointed at the center of the NIRC2 field-of-view for all observations. In May 2010, we successfully resolved CFBDSIR J1458+1013 into a tight binary using the moderate-band CH_4s filter, which has a central wavelength of 1.592 μm and a width of 0.126 μm . In July 2010, we obtained images with the J (1.25 μm), H (1.64 μm),

¹The T8 dwarf 2MASS J0939–24 has also been suggested to be an unresolved binary based on its absolute spectrophotometry (Burgasser et al. 2008; Leggett et al. 2009).

and K ($2.20\ \mu\text{m}$) filters from the Mauna Kea Observatories filter consortium (Simons & Tokunaga 2002; Tokunaga et al. 2002).

The images were analyzed in a similar fashion as our previous LGS papers (e.g. Liu et al. 2006, 2008). The raw images were reduced using standard methods of flat-fielding and sky-subtraction. After rejecting individual images of poor quality, we registered and stacked the data into a final mosaic. The binary’s flux ratios and relative astrometry were derived by fitting an analytic model of the point spread function (PSF) as the sum of two elliptical gaussians to the images of the binary in the mosaics. We did not correct the relative astrometry for instrumental optical distortion, as the size of the effect as predicted from a distortion solution by B. Cameron (priv. comm.) is insignificant compared to our measurements uncertainties. We adopted a pixel scale of $9.963 \pm 0.005\ \text{mas/pixel}$ and an orientation for the detector’s $+y$ axis of $+0.13 \pm 0.07^\circ$ for NIRC2 (Ghez et al. 2008).

To validate our measurements, we created myriad artificial binary stars from the science data themselves; given the large flux ratio of the binary, a scaled and shifted version of the primary star provides an excellent simulation of the data (e.g. Dupuy et al. 2009b). For each filter, our fitting code was applied to artificial binaries with similar separations and flux ratios as CFBDSIR J1458+1013AB over a range of position angles (PAs). The RMS scatter of the simulations were adopted as our measurement errors; the results also showed that any systematic offsets are small. The exceptions to this were the J and H -band separation measurements, where the average systematic offset from the simulations was slightly larger than the RMS scatter, and for these datasets we adopted the offset as the uncertainty. Table 1 presents our final Keck LGS measurements, and Figure 1 shows our Keck LGS images.

We use our measured flux ratios and the published JHK_S photometry from Delorme et al. (2010) to derive resolved IR colors and magnitudes for CFBDSIR J1458+1013AB on the MKO system. Delorme et al. report data using the K_S -band filter while our Keck LGS imaging used the K -band filter; to compute resolved K -band photometry, we synthesize an integrated-light color of $(K - K_S) = -0.17 \pm 0.02\ \text{mag}$ from the published spectra of ULAS J1238+09 (T8.5), Wolf 940B (T8.5), ULAS J0034–00 (T9), CFBDS J0059–01 (T9), and ULAS J1335+11 (T9) (Burningham et al. 2008, 2009; Warren et al. 2007; Delorme et al. 2008a). This is consistent with the color synthesized from the CFBDSIR J1458+1013AB spectrum itself (§ 2.3), but the signal-to-noise (S/N) in the K -band spectrum is quite low, so we use the average from the known T8.5 and T9 objects. To obtain the resolved CH_4s photometry from the published H -band data, we synthesizes a color $(CH_4s - H) = -0.47 \pm 0.03\ \text{mag}$ directly from the integrated-light spectrum of CFBDSIR J1458+1013AB. Table 3 presents the resolved photometry.

2.2. CFHT Infrared Astrometry

To determine the distance to CFBDSIR J1458+1013AB, we acquired seven epochs of J -band imaging in 2009 and 2010 spanning 1.07 years using the Canada-France-Hawaii 3.6-meter Telescope

on Mauna Kea, Hawai‘i. We used the facility wide-field near-IR camera WIRCam (Puget et al. 2004), which has four 2048×2048 Hawaii-2RG detectors, each with an approximate field-of-view of $10' \times 10'$. At each epoch, we placed the target near the center of the northeast detector. The data were taken with slightly different observing procedures as they originated from two independent programs: at 3 of the epochs, images of $60\text{-s} \times 6$ coadds were obtained at 10 dither positions, and at the other 4 epochs, single 60-s images were obtained at 11 dither positions. The median FWHM of the data was $0''.73$ (min/max of $0''.55/0''.80$). The target was always observed near transit, with a maximum deviation in airmass of 0.03. This reduces any systematic offsets in the target’s astrometry from the differential chromatic refraction between the late-T dwarf science target and the background stars to < 1 mas (Dupuy & Liu, in preparation), well below the measurement noise.

Our WIRCam astrometry pipeline is described in detail by Dupuy (2010) and Dupuy & Liu (in prep) and successfully generates parallaxes that are in accord with previously published results for L and T dwarfs. We use SExtractor (Bertin & Arnouts 1996) to generate an astrometric catalog of all the sources in every individual image. We then cross-match detections across dithered images and use the mean and rms of each source to determine its final position and error at that epoch; we exclude any source that has fewer than 7 detections or a S/N less than 7. We then cross-match these positions across different epochs, allowing for a full linear transformation in the astrometry to account for scale and orientation changes in the instrument. (WIRCam is installed and removed from the telescope for each observing run.) After an initial iteration, we remove any stars with large proper motions (> 50 mas/yr) or parallaxes ($> 3\sigma$) from the epoch-matching fit. Finally, we absolutely calibrate our astrometry by matching to 2MASS to determine the overall scale, orientation, and shear. For this target, 8 of our 72 reference stars were well-detected in 2MASS and had sufficiently low proper motion (< 30 mas/yr) to be used for absolute calibration.

We then fit for the proper motion and parallax of every source in the field. We measured a proper motion of 432 ± 6 mas/yr at a PA of $154.2 \pm 0.7^\circ$ for CFBDSIR J1458+1013, in good agreement with the Delorme et al. (2010) measurement of 444 ± 16 mas/yr and $157.5 \pm 2.1^\circ$ from seeing-limited images. CFBDSIR J1458+1013 was the only object we measured in the field with a significant parallax, 42.4 ± 4.5 mas relative to the reference stars. (To our knowledge, this is the faintest object outside the solar system with an optical or IR parallax measurement, cf., Marocco et al. 2010.) To account for the mean parallax of our reference stars, we used the Besançon model of the Galaxy (Robin et al. 2003) to simulate the distance distribution of sources in the direction of CFBDSIR J1458+1013 within the magnitude range of our images ($15.1 < J < 20.1$ mag). We find a mean parallax of 0.9 ± 0.1 mas from the Galaxy model, with the error accounting for the sampling variance due to the finite number of reference stars. This results in an absolute parallax of 43.3 ± 4.5 mas for CFBDSIR J1458+1013 (23.1 ± 2.4 pc), in good agreement with the original 23 pc photometric estimate by Delorme et al. (2010). The resulting tangential velocity (47 ± 5 km s $^{-1}$) is higher than the median for field T dwarfs, but not extraordinary given the observed velocity dispersion of the field objects (e.g. Vrba et al. 2004; Faherty et al. 2009). Table 2 contains our astrometry results.

2.3. VLT/X-Shooter Spectroscopy

We obtained integrated-light near-IR spectra of CFBDSIR J1458+1013AB with the X-Shooter spectrograph on VLT-UT2 (Program 085.C-0805). The observations were carried out in four 1-hour observing blocks (hereafter OB) from May 5 to July 9, 2010, achieving a total exposure time on target of 11700 sec, split into 8 A-B nods on the slit of 2×732 sec each. The slit width was $1.2''$, and the seeing varied between 0.8 – $1.0''$. We chose a large slit size, because direct acquisition of the target was impossible and we had to acquire using a blind offset from a reference source.

The spectra for each OB were reduced using the standard ESO X-Shooter pipeline (Modigliani et al. 2010), which produced a 2-dimensional, curvature-corrected spectrum of the NIR arm of X-Shooter (1.0 – $2.5 \mu\text{m}$). No signal was detected in the UVB and visible arm of the instrument. The trace was extracted using our own IDL procedures, using gaussian boxes in the spatial dimension at each wavelength. A similar gaussian extraction box was used at about 5 times the FWHM of the trace to obtain the noise spectrum of the sky. The resulting 1-dimensional spectrum from each science target OB was then divided by the spectra of telluric stars observed just before or after, reduced and extracted using the same pipelines.

The resulting 4 spectra from all the OBs were then median combined to produce the final science spectrum. Since the resulting spectrum (with $R \equiv \lambda/\Delta\lambda \approx 4300$) has low S/N and most analyses of late-T dwarfs have used much lower resolution spectra, we smoothed the spectra using a weighted average over 50 pixels in the wavelength dimension (corresponding to 3 and 5 nm at J -band and K -band, respectively), weighting by the inverse variance of the extracted sky spectrum. This approach uses the full spectral resolution of X-Shooter to give a much lower weight to wavelengths affected by telluric emission lines, thus improving the S/N with respect to simple unweighted binning using the average or median.

Given the large wavelength range covered by X-Shooter, seeing variation in the spectral direction can lead to wavelength-dependent slit losses. Therefore, we flux-calibrated the spectrum using JHK_S photometry of CFBDSIR J1458+1013 from Delorme et al. (2010) and Y -band data from the UKIDSS Data Release 8 ($Y = 20.58 \pm 0.21$ mag, on the Vega system). Following Delorme et al. (2008b), we applied small scaling factors to each of the broadband wavelength ranges so that the magnitudes derived from the CFBDSIR J1458+1013 spectrum matched the photometry. The final spectrum is shown in Figure 4.

3. Results

3.1. Proof of Companionship

Examination of the Digitized Sky Survey images shows no plausible optical counterpart if component B were a background object. Similarly, the z -band imaging from July 2004 presented in Delorme et al. (2010) shows no star to a depth of $z \sim 24$ mag, 2–3 mag deeper than expected

for a background M star if it had the near-IR magnitude of component B. In fact, the high proper motion of the source means that our two Keck epochs separated by 1.5 months are sufficient to confirm the two components are physically associated. (For the July 2010 epoch, we choose the Keck H -band astrometry, which has the smallest errors.) Figure 2 shows the large expected motion for component B if it were an object at infinite distance, given our measured proper motion and parallax for CFBDSIR J1458+1013. (The proper motion dominates over the parallax.) In contrast, the relative positions of the two components do not change between our observations. The length of the vector between the observed and predicted change is non-zero at 9.1σ . Thus, we conclude the two components are physically associated.

3.2. Integrated-Light Spectrum

3.2.1. Comparison with known late- T dwarfs

The integrated-light spectrum of CFBDSIR J1458+1013AB is very similar to other recent very late- T dwarf discoveries (Figure 4). As seen by its narrower continuum peak, its J -band spectrum shows slightly stronger absorption than the $T9$ dwarfs CFBDS J0059–01, ULAS J0034–00, and ULAS J1335+11 and is very close to the $T10$ dwarf UGPS J0722–05.² (We caution that spectral types later than $T8$ are an active topic of investigation, without a classification system established yet. For this discussion, we simply adopt the published types for these objects, which may ultimately change once a system is defined.) In the H band however, CFBDSIR J1458+1013 is more similar to the warmer objects, especially on the blue side of the peak. The absorption on the red side of the H -band is the strongest observed in any known brown dwarf (see the CH_4 - H index in Table 4). This might be due to enhanced collision induced absorption (CIA) of H_2 starting to suppress the H -band peak; this notion fits well with the strongly depressed K -band flux of CFBDSIR J1458+1013 compared to the other late- T dwarfs, where the strongest continuum absorber is CIA H_2 .

The suppression could be due to either strong gravity or low metallicity, and distinguishing between the two can be challenging (e.g. Liu et al. 2007). Using model atmospheres, Burgasser et al. (2006a) and Leggett et al. (2007) show that the shape of the Y -band continuum is more metallicity-dependent than gravity-dependent (though their two sets of models show different amplitudes for these effects). The main absorbers on the blue side of the Y -band peak are the pressure broadened wings of the K I and Na I fundamental doublets, which naturally decrease with lower metallicity; more metal-rich models also have the Y -band peak at redder wavelengths and the overall Y -band

²Lucas et al. (2010) report the presence of an unidentified, narrow absorption feature at $1.275 \mu\text{m}$ in the spectrum of UGPS J0722–05. They suggest it arises from H_2O or HF . Figure 4 suggests it may also be present in CFBDSIR J1458+1013AB. However, while the detection is significant in terms of S/N, it appears much broader than in the UGPS J0722–05 spectrum. Also, Lucas et al. reports a second absorption feature at $1.282 \mu\text{m}$, which coincides with a local peak in the CFBDSIR J1458+1013AB spectrum. Thus our spectra do not confirm either of these proposed features.

flux being fainter. The observed Y -band spectra of CFBDSIR J1458+1013AB does not show any strong differences with UGPS J0722–05 and CFBDS J0059–01 (Figure 4), though the peak might be slightly redder than the other two objects, perhaps hinting at a greater metallicity (though this would be discrepant with the highly suppressed K -band). Overall, we favor the higher gravity explanation, though a better spectrum at shorter wavelengths would help to investigate this further.

Taken altogether, the spectrum of CFBDSIR J1458+1013AB shows that this object is slightly earlier than UGPS J0722–05 and possibly higher gravity, but later than the known T9 dwarfs. Thus, we provisionally assign a spectral type of T9.5, though of course it may turn out to be earlier or later type, depending on the future development of classification for such cool objects.

3.2.2. Spectral index analysis with solar-metallicity models

To quantify the absorption features of CH_4 , H_2O , CIA H_2 , and possibly NH_3 , we calculated spectral indices previously used for T dwarfs (Burgasser et al. 2006b; Warren et al. 2007; Delorme et al. 2008a). The measurements (Table 4) indicate that CFBDSIR J1458+1013A has some of the strongest absorption features seen in the near-IR spectra of late T dwarfs, exceeded by only UGPS J0722–05 for the W_J and $\text{NH}_3\text{-H}$ indices. Given the ≈ 2 magnitudes flux difference between component A and B, it is reasonable to consider the integrated spectrum is dominated by the primary (as discussed below).

We use the solar-abundance BT-Settl-2009 models (Allard & Freytag 2010) to estimate T_{eff} and $\log(g)$ for component A from the index measurements. We compensate for the systematic errors of the models (e.g. Leggett et al. 2007; Liu et al. 2008) by scaling their index predictions to match those measured for the T8.5 benchmark Wolf 940B (Burningham et al. 2009). Its high quality spectrophotometry, parallax, and age estimate from its primary star enable a precise estimate of its properties using evolutionary models ($T_{\text{eff}} = 575$ K; $\log(g) = 4.75$, $[\text{M}/\text{H}] = 0$ from Burningham et al. 2009; see also Leggett et al. 2010a). With this approach, the temperatures and gravities for the $>\text{T8}$ dwarfs derived from an index-index plot broadly agree with the values derived from the analysis of their full near-IR spectra (Burgasser et al. 2006a; Warren et al. 2007; Delorme et al. 2008a; Burningham et al. 2008; Lucas et al. 2010).

Since the systematic errors in the models in this low-temperature regime are likely much larger than the measurement errors, we use the model grid only for relative estimates of temperature and gravity differences among the late-T dwarfs, not absolute measurements. Figure 5 indicates that CFBDSIR J1458+1013A is as cool as UGPS J0722–05 and $\gtrsim 50$ K or more cooler than the other $>\text{T8}$ dwarfs. (The caveat is that the model analysis assumes a single metallicity for all the objects, consistent with the similarity in Y -band shapes discussed above.) The plot also puts CFBDSIR J1458+1013A at a higher ($\gtrsim 0.5$ dex) surface gravity than the other objects, as expected from the highly suppressed K -band flux. The higher gravity suggests that CFBDSIR J1458+1013A is older and higher mass than UGPS J0722–05, consistent with their relative tangential velocities

($47 \pm 5 \text{ km s}^{-1}$ and $19 \pm 3 \text{ km s}^{-1}$, respectively). Of course, tangential velocities are only a statistical proxy for age so this comparison should be treated accordingly.

To assess the impact of component B on the integrated-light spectrum, we used the BT-Settl-2009 model atmospheres to create composite spectra. We chose models with 600–700 K for the primary and 400–500 K for the secondary, matching pairs of models with 200–250 K temperature differences and the same surface gravity. The pairs of spectra were scaled to agree with the observed J -band or H -band flux ratio and summed to form artificial composites. We then added noise based on the measured S/N of the VLT spectrum and measured the same indices. We found that the blended composites had very similar index values as the input primary spectrum alone, with systematic effects at the 5–20% level, typically 10%. Such amplitudes are not sufficient to affect the interpretation of Figure 5.

3.2.3. Model atmosphere fitting

To further place CFBDSIR J1458+1013AB in context, we perform a homogeneous comparison of the near-IR spectra of very late-T dwarfs to low-temperature atmospheric models. We restrict our analysis to $\geq T8$ dwarfs with parallaxes, excluding the aforementioned possible binary T8 dwarf 2MASS J0939–24, but also include two benchmark T7.5 dwarfs (Table 5). We use the published J -band photometry to establish the absolute flux calibration of the spectra, again assuming the primary dominates the integrated-light spectrum. For CFBDSIR J1458+1013AB, we again assumed that the integrated-light spectrum is dominated by component A and normalized it using the resolved J -band photometry of component A.

We fit three grids of atmospheric models: (1) the Ames-Cond models (Allard et al. 2001) spanning $T_{\text{eff}} = 400 - 1200 \text{ K}$ ($\Delta T_{\text{eff}} = 100 \text{ K}$) and $\log(g) = 4.0 - 6.0$ ($\Delta \log(g) = 0.5$); (2) the Tucson models (Burrows et al. 2003, hereafter BSL03), which are irregularly gridded between $T_{\text{eff}} \approx 150 - 850 \text{ K}$ and $\log(g) \approx 3.3 - 4.8$ (cgs); and (3) the aforementioned BT-Settl-2009 models spanning 400–1200 K and $\log(g) = 4.0 - 6.0 \text{ dex}$ ($\Delta T_{\text{eff}} = 50 \text{ K}$ above 600 K and 100 K below 600 K). All grids are for solar metallicity compositions and chemical equilibrium. The models were gaussian smoothed to the resolution of the data and interpolated onto the wavelength grid of the observed spectrum.

The atmospheric models have known systematic errors, particularly in the Y -band and the red side of the H -band as a result of imperfect modeling of the pressure-broadened K I doublet in the far-red and the incomplete list of CH_4 lines, respectively. We therefore restrict our fits to the 1.15–1.35 μm , 1.45–1.6 μm , and 1.95–2.25 μm spectral regions. The model emergent spectra are scaled to the flux calibrated spectra by minimizing the χ^2 statistic (e.g., Equation 5 and 6 of Bowler et al. 2009). For observed spectra without measurement errors (CFBDS J0059–01 and UGPS J0722–05) we perform a least-squares fit to the data (Equation 1 of Stephens et al. 2009 with $w_i=1$, and the scaling factor is solved for by equating the derivative of G_1 with zero).

The best-fitting models are summarized in Table 5 and plotted in Figure 6. The Ames-Cond models yield effective temperatures between 700–800 K and a gravity of 4.5 dex for almost all objects; the temperatures for the latest-type objects are ≈ 100 –200 K hotter than analyses from their discovery papers (which use variants of the BT-Settl models). The BSL03 models typically produce much cooler temperatures (420–800 K) and somewhat higher gravities (4.6–4.8 dex), with the results for the earlier-type objects often at the edge of the model grid, indicating a broader set of models is probably needed. The BT-Settl-2009 model results are usually intermediate between those from the other two models. The fits show that CFBDS J0059–01, CFBDSIR J1458+1013AB, and UGPS J0722–05 are the three coldest objects in the sample, with the Ames-Cond models indicating all have comparable temperatures while the BSL03 and BT-Settl-2009 models indicate that CFBDSIR J1458+1013AB is the warmest. (Note that in terms of the absolute values derived from the fitting, the analysis in the Appendix on the resulting spectroscopic distances suggests that the temperatures may be somewhat overestimated.)

Again, to assess the effect of component B on the analysis of the integrated-light spectrum, we took the artificial noisy composite spectra described in § 3.2.2 and applied the same model atmosphere fitting procedure. We found that the T_{eff} ’s determined for the composite spectra were at worst 50 K colder than those of the input primary spectrum alone, and often the same. The fitted surface gravities were the same for the composites and the primary spectrum. Thus, the blended light from the much fainter secondary appears to have little consequence for our analysis, as expected.

We also examine another method to derive physical properties from atmospheric models. Although the distance estimates using the scaling factor $(R/d)^2$ may differ substantially from the true distances, the known distance can be used in combination with the scaling factor, a grid of radii, and a likely age range to infer a temperature and mass range for the object. This is effectively using the scaling factor as a proxy for temperature, and it has the benefit of relying on the absolute level of the model emergent flux density rather than the detailed shape of the synthetic spectrum, which may have systematic errors. Using the results from Table 5, we compute the range of effective temperatures and masses for the three sets of models. The results are shown in Table 6 assuming an age range of 1–10 Gyrs, except for Ross 458C where we assume an age of 0.1–1.0 Gyr (Goldman et al. 2010). The BSL03 models are limited at high gravities by an upper mass cutoff of $25 M_{\text{Jup}}$ so they only provide lower limits on T_{eff} and mass. The resulting range of temperatures and masses is similar to those estimated in previous work (Liu et al. 2007; Burningham et al. 2008; Delorme et al. 2008a). This analysis indicates that CFBDSIR J1458+1013A has a similar effective temperature (540–660 K) and mass (12–42 M_{Jup}) to the T9 dwarfs ULAS J0034–00 and ULAS J1335+11, with CFBDS J0059–01 and UGPS J0722–05 being perhaps slightly cooler, in accord with the relative ordering of their absolute magnitudes.

3.3. Resolved Colors and Magnitudes

In accord with the integrated-light spectrum, the near-IR colors of component A are similar to those of the known T8–T10 dwarfs, with its $(H - K)$ color of -0.45 ± 0.26 mag being somewhat bluer than most objects, though the uncertainty is large. As discussed above, the bluer color is likely due to a higher surface gravity (i.e., an older age) compared to most other late-T dwarfs.

Our near-IR parallax for the system provides the absolute magnitudes for component B and reveals its extreme nature. Compared to the T10 dwarf UGPS J0722–05, CFBDSIR J1458+1013B is fainter by 1.4 ± 0.4 , 1.9 ± 0.3 , and 2.0 ± 0.4 mag in its JHK absolute magnitudes, respectively. Being significantly fainter than previously known brown dwarfs (Figure 7), the properties of CFBDSIR J1458+1013B provide a first look at the empirical trends beyond spectral type T10, especially enlightening given the uncertainties in model atmosphere predictions for such cold objects (e.g. Burrows et al. 2003). The very blue ($CH_4s - H$) color indicates strong CH_4 absorption persists at H -band, comparable to the known T8–T9 dwarfs which have a $(CH_4s - H) \approx -0.5$ to -0.6 mag (e.g., Figure 2 of Tinney et al. 2005 and Section 3.2 of Liu et al. 2008).

The near-IR colors of CFBDSIR J1458+1013B are very blue (Figure 8), with its $H - K$ color is similar and the $J - K$ color slightly bluer than previously known T dwarfs (except for the T6p dwarf 2MASS 0937+29, which is suspected to have low metallicity; Burgasser et al. 2002). For its absolute magnitude, its $J - K$ color is much redder than those predicted by the Lyon/Cond (Baraffe et al. 2003) and Saumon & Marley (2008, hereafter SM08) models, and to a lesser degree the BSL03 models as well. The most intriguing behavior is seen in $J - H$, where the blueward trend with spectral type among the T dwarfs appears to reach an inflection point with the T8–T10 dwarfs, and then CFBDSIR J1458+1013B continues to bluer colors.

3.4. Physical Properties from Evolutionary Models

How much cooler is CFBDSIR J1458+1013B than previously known late-T dwarfs? Using its absolute magnitudes as a simple proxy for L_{bol} (i.e., assuming the same bolometric corrections as other T9–T10 objects), its L_{bol} is a factor of $\approx 4\text{--}6\times$ smaller. Old brown dwarfs have essentially constant radii, so this would correspond to an object that is a factor of ≈ 1.5 cooler. The T9–T10 objects have estimated T_{eff} of 500–600 K from model atmosphere fitting and their bolometric luminosities (Leggett et al. 2009, 2010a; Marocco et al. 2010; Lucas et al. 2010); simple scaling would then make CFBDSIR J1458+1013B $\approx 350\text{--}400$ K.

With L_{bol} estimates for the individual components and an assumed age, evolutionary models can fully determine the remaining physical properties of the two components (e.g. Saumon et al. 2000). This approach is desirable as predictions of L_{bol} are less dependent on the assumed model atmospheres than predictions of the absolute magnitudes (Chabrier et al. 2000b; Saumon & Marley 2008). This approach has also been widely used for temperature determinations for field L and

T dwarfs (e.g. Golimowski et al. 2004). Of course, such estimates should be treated with caution, since CFBDSIR J1458+1013B resides in a low-temperature, low-luminosity regime where the models have not been tested against any observations. (In the case of L dwarfs, Dupuy et al. 2009a have found that for a given luminosity and assumed age, the evolutionary models may overestimate the masses.)

To estimate L_{bol} , we adopt J -band bolometric corrections from the coolest T dwarfs with parallaxes: ULAS J0034–00 (T9; $BC_J = 1.96 \pm 0.11$ mag), CFBDS J0059–01 (T9; 1.87 ± 0.21 mag), and ULAS J1335+11 (T9; 1.82 ± 0.09 mag) from Marocco et al. (2010), and UGPS J0722–05 (T10; 1.36 ± 0.21 mag) from Lucas et al. (2010). The unweighted average is 1.75 ± 0.27 mag, and we apply this to both components of CFBDSIR J1458+1013AB. The resulting values for L_{bol}/L_{\odot} are $(1.1 \pm 0.4) \times 10^{-6}$ and $(2.0 \pm 0.9) \times 10^{-7}$ for components A and B, respectively. In comparison, CFBDS J0059–0114 and UGPS J0722–05 have $L_{\text{bol}}/L_{\odot} = (7.2 \pm 1.2) \times 10^{-7}$ and $(9.2 \pm 3.1) \times 10^{-7}$, respectively, making CFBDSIR J1458+1013B a factor of ≈ 4 –5 less luminous than these two objects.

Table 3 presents the derived physical quantities for ages of 1.0 and 5.0 Gyr. The L_{bol} uncertainty is propagated into the calculations in a Monte Carlo fashion. The inferred temperature of component B is exceptionally low, 360–380 K from the Lyon/COND models and 350–380 K from the Burrows et al. (1997) ones. Including the random uncertainties from the Monte Carlo results, we adopt a final T_{eff} estimate of 370 ± 40 K. The model-derived mass is 6–14 (7–17) for the Lyon/COND (Burrows) models, possibly placing the object below the notional $13 M_{\text{Jup}}$ dividing line between planets and brown dwarfs based on the deuterium-burning limit. Overall, the physical properties of CFBDSIR J1458+1013B overlap those of the gas-giant planets found from radial velocity surveys. In fact, both components of CFBDSIR J1458+1013AB would reside in the planetary-mass regime and have retained their initial deuterium abundance for ages of $\lesssim 1$ Gyr.

To gauge the systematic effects, we also compute physical properties using the BSL03 models, which provide predictions for absolute magnitudes. (The Lyon/COND models also provide absolute magnitudes, but these disagree more strongly with the color-magnitude data in Figure 7.) We compare the BSL03 models to the J -band observations, as this bandpass represents the peak of the near-IR SED. (Note that this is largely equivalent to using the BSL03 atmospheric models for their bolometric corrections.) The results are listed in Table 3 and agree reasonably well with those derived from L_{bol} and assuming the bolometric corrections from the known T9–T10 dwarfs.

Measuring the differential deuterium abundance would help constrain the age of the system, analogous to the binary lithium test proposed by Liu & Leggett (2005). The deuterium depletion timescales are long for such low-mass objects, so the exact age at which they become fully depleted is fuzzy. Using a finely interpolated version of the Lyon/COND models (Baraffe et al. 2003) and constrained by the observed luminosity of each component, we find that the full range of 99% to 0% deuterium content for the primary is 0.5–1.3 Gyr, while the 99–0% deuterium range for the secondary is 2.3–5.4 Gyr. Thus, for ages of < 0.5 Gyr, both components retain their deuterium and would have masses of < 9 and $< 4 M_{\text{Jup}}$. Between 0.5–2 Gyr, the primary is depleted but the

secondary retains its deuterium. And for ages older than 2 Gyr both components are depleted and are >20 and $>10 M_{\text{Jup}}$. (Allers et al. 2010 report the discovery of a young field L dwarf binary whose estimated luminosities and age indicate that the two components may be in the process of differential deuterium depletion.) Note that the deuterium abundance is expected to be difficult to measure (Chabrier et al. 2000a). An additional complication is the theoretical predictions for the D-burning limit depend on the metallicity, initial D and He abundances, and atmospheric boundary conditions and can range from ≈ 11 – $14 M_{\text{Jup}}$ (Spiegel et al. 2010).

3.5. Orbital Period

To estimate the orbital period of the binary, we adopt the statistical conversion factor between projected separation and true semi-major axis from Dupuy & Liu (2011). They offer several choices, based on the underlying eccentricity distribution and degree of completeness to finding binaries by imaging (“discovery bias”). We adopt the eccentricity distribution from their compilation of ultracool visual binaries with high quality orbits and assume their case of modest discovery bias, namely that the smallest possible projected separation for detection is half the semi-major axis. This gives a multiplicative correction factor of $1.07^{+0.42}_{-0.27}$ (68.3% confidence limits) for converting the projected separation into semi-major axis (compared to $1.10^{+0.92}_{-0.35}$ for a uniform eccentricity distribution with no discovery bias). The resulting orbital period estimates range from 20–35 years for ages of 1.0–5.0 Gyr, albeit with significant uncertainties (Table 3). Dynamical masses for ultracool binaries may be realized from orbital monitoring covering $\gtrsim 30\%$ of the period (e.g. Bouy et al. 2004; Liu et al. 2008; Dupuy et al. 2009). Thus, CFBDSIR J1458+1013AB warrants continued high angular resolution imaging to determine its visual orbit, which can then be combined with the parallax to directly measure its total mass.

4. Discussion: Y or Y not?

Definition of the Y spectral type awaits discovery of objects whose spectra are unambiguously different from the T dwarfs, in the same fashion as the distinction between M and L dwarfs and between L and T dwarfs. The near-IR spectral progression observed for the T8–T10 dwarfs is subtle, as the CH_4 bands are nearly fully absorbed. Such late-type objects are distinguished from each other by only modest changes in the shape of the near-IR flux peaks (e.g. Delorme et al. 2008a; Burningham et al. 2008; Lucas et al. 2010), though the thermal-IR ($\lambda > 3 \mu\text{m}$) colors are more distinctive (Leggett et al. 2010b).

Recent work has highlighted near-IR spectral features that might arise from NH_3 (Saumon et al. 2007; Delorme et al. 2008a; Lucas et al. 2010) but not in a definitive fashion. Model atmospheres suggest the onset of NH_3 at ≈ 600 K but also indicate the effect could be indistinctive (Burrows et al. 2003; Leggett et al. 2007). The emergence of narrow intra-band features, possibly linked to NH_3

absorption, is difficult to disentangle from the effects of differing gravities and metallicities. Also, the available opacities for CH_4 and H_2O are known to be incomplete, complicating the identification of new species. In short, the current census does not seem to compel the use of the Y spectral type. (Of course, future identification of unambiguous examples may lead to re-classification of some known objects as early Y dwarfs.)

Overall, CFBDSIR J1458+1013B is the most promising candidate to date for the hypothesized Y spectral class, given its extremely low luminosity, atypical near-IR colors, and cold inferred temperature. While spectroscopy is needed to place it in full context with the known T dwarfs, the singular nature of this object is unambiguous, thanks to our parallax measurement. CFBDSIR J1458+1013B is ≈ 1.5 – 2.0 magnitudes less luminous in the near-IR than any previously known brown dwarf and therefore is cooler than any known brown dwarf.³ For reference, two magnitudes in absolute magnitude spans most of the T dwarf sequence, from about T0 to T6 (e.g. Liu et al. 2006; Marocco et al. 2010). On this basis alone, this object is a significant leap. For comparison, the T10 dwarf UGPS J0722–05 is only ≈ 0.2 mag fainter than CFBDS J0059–01 in absolute magnitude, and among the small sample of $>\text{T}8$ dwarfs, the differences in absolute magnitudes are $\lesssim 0.5$ mag between objects. For this reason, a spectral type estimate of $>\text{T}10$ seems appropriate for CFBDSIR J1458+1013B, as opposed to $\geq \text{T}10$. (A naive extrapolation of the linear trend in absolute magnitude with T subclass would make the object around T12.) While it could be that near-IR spectra changes so slowly with temperature that a broad luminosity range of objects all appear to be the same as the UGPS J0722–05, this seems unlikely given the behavior of the hotter T subclasses.

Regardless of its final spectral classification, CFBDSIR J1458+1013B provides a gateway into new processes in low-temperature atmospheres. Models by Burrows et al. (2003) predict the disappearance of the very broad sodium ($0.59\ \mu\text{m}$) and potassium ($0.77\ \mu\text{m}$) resonance lines at $T_{\text{eff}} \approx 450 - 500$ K, comparable to the estimated temperature of CFBDSIR J1458+1013B. (See also Leggett et al. 2007.) This change might be detected from resolved far-red optical spectroscopy and photometry from *HST*. Also, Burrows et al. predict the formation of photospheric water clouds at ≈ 400 – 500 K (with hotter temperatures for higher surface gravities), though this phenomenon has little impact on their model emergent spectra. At ≈ 300 – 400 K, they predict the cessation of the blueward trend in near-IR colors with decreasing temperature. Such signatures might be delineated with resolved multi-band far-red optical and near-IR data of CFBDSIR J1458+1013AB. Our current measurements indicate that the trends of near-IR colors with spectral type continue without enormous changes, but that they may be non-monotonic. Indeed, the subtle changes seen in the near-IR SEDs of late-T dwarfs, combined with the strong alkali line depletion predicted at

³From a deep *Spitzer* extragalactic survey, Eisenhardt et al. (2010) have identified a very faint, low/no proper motion source whose exceptionally red thermal-IR colors and non-detection in the near-IR suggest a $\lesssim 450$ K object at $\gtrsim 70$ pc. Direct comparison with CFBDSIR J1458+1013B is not possible, since there are no photometric detections in common between the two objects. Their object’s *H*-band non-detection ($H > 24.2$ mag) is consistent with CFBDSIR J1458+1013B, which would be $H = 24.9$ mag at 70 pc.

$\lesssim 500$ K, suggest that far-red optical wavelengths may become valuable for spectral classification of the coolest new discoveries.

The fact that CFBDSIR J1458+1013B resides in a binary system of known distance offers additional future opportunities for understanding the coldest brown dwarfs. The estimated mass ratio ($q \approx 0.5$) is uncommonly small compared to most field systems, representing only $\lesssim 5\%$ of known binaries (Liu et al. 2010). Measuring accurate L_{bol} and T_{eff} for the two components could test the joint accuracy of evolutionary and atmospheric models under the constraint of coevality (e.g. White et al. 1999; Kraus & Hillenbrand 2009; Liu et al. 2010). Furthermore, given their identical composition and similar surface gravities, comparing the SEDs of the two components directly probes the influence of decreasing effective temperature, without other physical parameters to consider. So the binary may yield valuable insights about the transition from T dwarfs to Y dwarfs. Finally, the estimated orbital period of ≈ 20 –30 years means a direct dynamical mass estimate is feasible over the next several years; such a mass benchmark would provide a stringent test of substellar models. A dynamical mass would also help to demarcate the low-mass limit for star formation.

It is a pleasure to thank Jim Lyke, Gary Punawai, Cynthia Wilburn, and the Keck Observatory staff for assistance with the LGS AO observing and the staffs of CFHT and VLT for carrying out the queue imaging and spectroscopy. We thank Sandy Leggett and Didier Saumon for making published results readily available and thank Kathleen Brandt for assistance while this paper was being written. Our research has employed the 2MASS data products; NASA’s Astrophysical Data System; the SIMBAD database operated at CDS, Strasbourg, France; and the SpeX Prism Spectral Libraries maintained by Adam Burgasser at <http://www.browndwarfs.org/spexprism>. MCL, TJD, and BPB acknowledge support for this work from NSF grants AST-0507833 and AST-0909222. Support for this work to TJD was partially provided by NASA through Hubble Fellowship grant #HF-51271.01-A awarded by the Space Telescope Science Institute, which is operated by the Association of Universities for Research in Astronomy, Inc., for NASA, under contract NAS 5-26555. Finally, the authors wish to recognize and acknowledge the very significant cultural role and reverence that the summit of Mauna Kea has always had within the indigenous Hawaiian community. We are most fortunate to have the opportunity to conduct observations from this mountain.

Facilities: Keck II Telescope (LGS AO, NIRC2), Canada-France-Hawaii Telescope (WIRCAM), VLT-UT2 (X-Shooter)

A. Spectroscopic Distance Estimates for Late-T Dwarfs

Using the fitting results from § 3.2.3, we can test the accuracy of atmospheric models by comparing the measured distances to model-derived spectroscopic distances following the method of Bowler et al. (2009). The scaling factor between the model emergent spectra and the observed

spectra is equal to $(R/d)^2$, so if a radius is known (or assumed) then the distance can be computed. Bowler et al. estimated distances to four late-M and L subdwarfs using this method and found agreement to within $\sim 10\%$ of published parallaxes. Several subsequent studies have used this technique to estimate distances for late-T dwarfs without parallaxes (e.g. Mainzer et al. 2011), but this method has yet to be tested for such objects. We do so now with the Ames-Cond, BSL03, and BT-Settl-2009 models.

To compute model-derived spectroscopic distances, for the Ames-Cond and BT-Settl-2009 atmospheric models we use radii from the companion grid of Lyon/Cond evolutionary models (Baraffe et al. 2003) interpolated across ages, effective temperatures, and surface gravities. For the BSL03 models, we use a power law fit for the radius as a function of T_{eff} and $\log(g)$ from the Burrows et al. (1997) evolutionary models (Equation 1 of BSL03). We compute errors in the spectroscopic distances from two components. (1) Measurement uncertainties from the finite S/N of the spectra and the absolute flux calibration from the J -band photometry are accounted for in a Monte Carlo fashion. We adopt the median and RMS of the resulting distributions as one version of the results. (2) In addition, we account for systematic uncertainties in the models by assuming normally distributed errors of 50 K and 0.25 dex in the fitted T_{eff} and $\log(g)$. The standard deviation of the resulting spectroscopic distance distribution is reported along with the uncertainty due to random errors.

Table 5 summarizes the results, with both sets of uncertainty calculations. The agreement between the spectroscopic distances and the parallactic distance range from $\approx 10\%$ to about a factor of two, with no apparent trend in accuracy with distance, spectral type, or model grid. The large scatter likely arises from the sensitivity of the distance estimate to the best-fitting model T_{eff} . The typically larger spectroscopic distances compared to parallactic distances imply an over-estimate of T_{eff} in the best-fitting model, because the scaling factor is highly sensitive to temperature (absolute flux level) and very weakly dependent on gravity.

REFERENCES

- Allard, F., & Freytag, B. 2010, *Highlights of Astronomy*, 15, 756
- Allard, F., Hauschildt, P. H., Alexander, D. R., Tamanai, A., & Schweitzer, A. 2001, *ApJ*, 556, 357
- Allers, K. N., Liu, M. C., Dupuy, T. J., & Cushing, M. C. 2010, *ApJ*, in press
- Baraffe, I., Chabrier, G., Barman, T. S., Allard, F., & Hauschildt, P. H. 2003, *A&A*, 402, 701
- Becklin, E. E., & Zuckerman, B. 1988, *Nature*, 336, 656
- Bertin, E., & Arnouts, S. 1996, *A&AS*, 117, 393
- Bouy, H., et al. 2004, *A&A*, 423, 341

- Bowler, B. P., Liu, M. C., & Cushing, M. C. 2009, *ApJ*, 706, 1114
- Burgasser, A. J., Burrows, A., & Kirkpatrick, J. D. 2006a, *ApJ*, 639, 1095
- Burgasser, A. J., Geballe, T. R., Leggett, S. K., Kirkpatrick, J. D., & Golimowski, D. A. 2006b, *ApJ*, 637, 1067
- Burgasser, A. J., Tinney, C. G., Cushing, M. C., Saumon, D., Marley, M. S., Bennett, C. S., & Kirkpatrick, J. D. 2008, *ApJ*, 689, L53
- Burgasser, A. J., et al. 2000, *ApJ*, 531, L57
- . 2002, *ApJ*, 564, 421
- Burningham, B., et al. 2008, *MNRAS*, 391, 320
- . 2009, *MNRAS*, 395, 1237
- . 2010, *MNRAS*, 404, 1952
- Burrows, A., Sudarsky, D., & Lunine, J. I. 2003, *ApJ*, 596, 587
- Burrows, A., et al. 1997, *ApJ*, 491, 856
- Chabrier, G., Baraffe, I., Allard, F., & Hauschildt, P. 2000a, *ApJ*, 542, L119
- . 2000b, *ApJ*, 542, 464
- Dahn, C. C., et al. 2002, *AJ*, 124, 1170
- Delorme, P., et al. 2008a, *A&A*, 482, 961
- . 2008b, *A&A*, 484, 469
- . 2010, *A&A*, 518, A39
- Dupuy, T. J. 2010, PhD thesis, University of Hawaii
- Dupuy, T. J., & Liu, M. C. 2011, *ApJ*, 733, 122
- Dupuy, T. J., Liu, M. C., & Bowler, B. P. 2009, *ApJ*, 706, 328
- Dupuy, T. J., Liu, M. C., & Ireland, M. J. 2009a, *ApJ*, 692, 729
- . 2009b, *ApJ*, 699, 168
- Eisenhardt, P. R. M., et al. 2010, *AJ*, 139, 2455
- Faherty, J. K., Burgasser, A. J., Cruz, K. L., Shara, M. M., Walter, F. M., & Gelino, C. R. 2009, *AJ*, 137, 1

- Ghez, A. M., et al. 2008, *ApJ*, 689, 1044
- Goldman, B., Marsat, S., Henning, T., Clemens, C., & Greiner, J. 2010, *MNRAS*, 405, 1140
- Golimowski, D. A., et al. 2004, *AJ*, 127, 3516
- Harrington, R. S., & Dahn, C. C. 1980, *AJ*, 85, 454
- Janson, M., et al. 2011, *ApJ*, 728, 85
- Kirkpatrick, J. D., et al. 1999, *ApJ*, 519, 802
- Kraus, A. L., & Hillenbrand, L. A. 2009, *ApJ*, 704, 531
- Leggett, S. K., Saumon, D., Burningham, B., Cushing, M. C., Marley, M. S., & Pinfield, D. J. 2010a, *ApJ*, 720, 252
- Leggett, S. K., et al. 2007, *ApJ*, 667, 537
- Leggett, S. K., et al. 2009, *ApJ*, 695, 1517
- . 2010b, *ApJ*, 710, 1627
- Liu, M. C., Dupuy, T. J., & Ireland, M. J. 2008, *ApJ*, 689, 436
- Liu, M. C., Dupuy, T. J., & Leggett, S. K. 2010, *ApJ*, 722, 311
- Liu, M. C., & Leggett, S. K. 2005, *ApJ*, 634, 616
- Liu, M. C., Leggett, S. K., & Chiu, K. 2007, *ApJ*, 660, 1507
- Liu, M. C., Leggett, S. K., Golimowski, D. A., Chiu, K., Fan, X., Geballe, T. R., Schneider, D. P., & Brinkmann, J. 2006, *ApJ*, 647, 1393
- Lucas, P. W., et al. 2010, *MNRAS*, 408, L56
- Luhman, K. L., et al. 2007, *ApJ*, 654, 570
- Mainzer, A., et al. 2011, *ApJ*, 726, 30
- Marocco, F., et al. 2010, *A&A*, 524, A38
- McCaughrean, M. J., Close, L. M., Scholz, R.-D., Lenzen, R., Biller, B., Brandner, W., Hartung, M., & Lodieu, N. 2004, *A&A*, 413, 1029
- Modigliani, A., et al. 2010, in Presented at the Society of Photo-Optical Instrumentation Engineers (SPIE) Conference, Vol. 7737, Society of Photo-Optical Instrumentation Engineers (SPIE) Conference Series
- Monet, D. G., et al. 2003, *AJ*, 125, 984

- Mugrauer, M., Seifahrt, A., Neuhäuser, R., & Mazeh, T. 2006, MNRAS, 373, L31
- Nakajima, T., Oppenheimer, B. R., Kulkarni, S. R., Golimowski, D. A., Matthews, K., & Durrance, S. T. 1995, Nature, 378, 463
- Puget, P., et al. 2004, in Society of Photo-Optical Instrumentation Engineers (SPIE) Conference Series, Vol. 5492, Society of Photo-Optical Instrumentation Engineers (SPIE) Conference Series, ed. A. F. M. Moorwood & M. Iye, 978–987
- Robin, A. C., Reylé, C., Derrière, S., & Picaud, S. 2003, A&A, 409, 523
- Saumon, D., Geballe, T. R., Leggett, S. K., Marley, M. S., Freedman, R. S., Lodders, K., Fegley, B., J., & Sengupta, S. K. 2000, ApJ, 541, 374
- Saumon, D., & Marley, M. S. 2008, ApJ, 689, 1327
- Saumon, D., et al. 2007, ApJ, 656, 1136
- Scholz, R. 2010a, A&A, 510, L8
- Scholz, R.-D. 2010b, A&A, 515, A92
- Simons, D. A., & Tokunaga, A. 2002, PASP, 114, 169
- Smart, R. L., et al. 2010, A&A, 511, A30
- Spiegel, D. S., Burrows, A., & Milsom, J. A. 2010, ArXiv e-prints, (ApJ, in press)
- Stephens, D. C., et al. 2009, ApJ, 702, 154
- Thalmann, C., et al. 2009, ApJ, 707, L123
- Tinney, C. G., Burgasser, A. J., & Kirkpatrick, J. D. 2003, AJ, 126, 975
- Tinney, C. G., Burgasser, A. J., Kirkpatrick, J. D., & McElwain, M. W. 2005, AJ, 130, 2326
- Tokunaga, A. T., Simons, D. A., & Vacca, W. D. 2002, PASP, 114, 180
- van Dam, M. A., et al. 2006, PASP, 118, 310
- van Leeuwen, F. 2007, A&A, 474, 653
- Vrba, F. J., et al. 2004, AJ, 127, 2948
- Warren, S. J., et al. 2007, MNRAS, 381, 1400
- White, R. J., Ghez, A. M., Reid, I. N., & Schultz, G. 1999, ApJ, 520, 811
- Wizinowich, P. L., et al. 2006, PASP, 118, 297

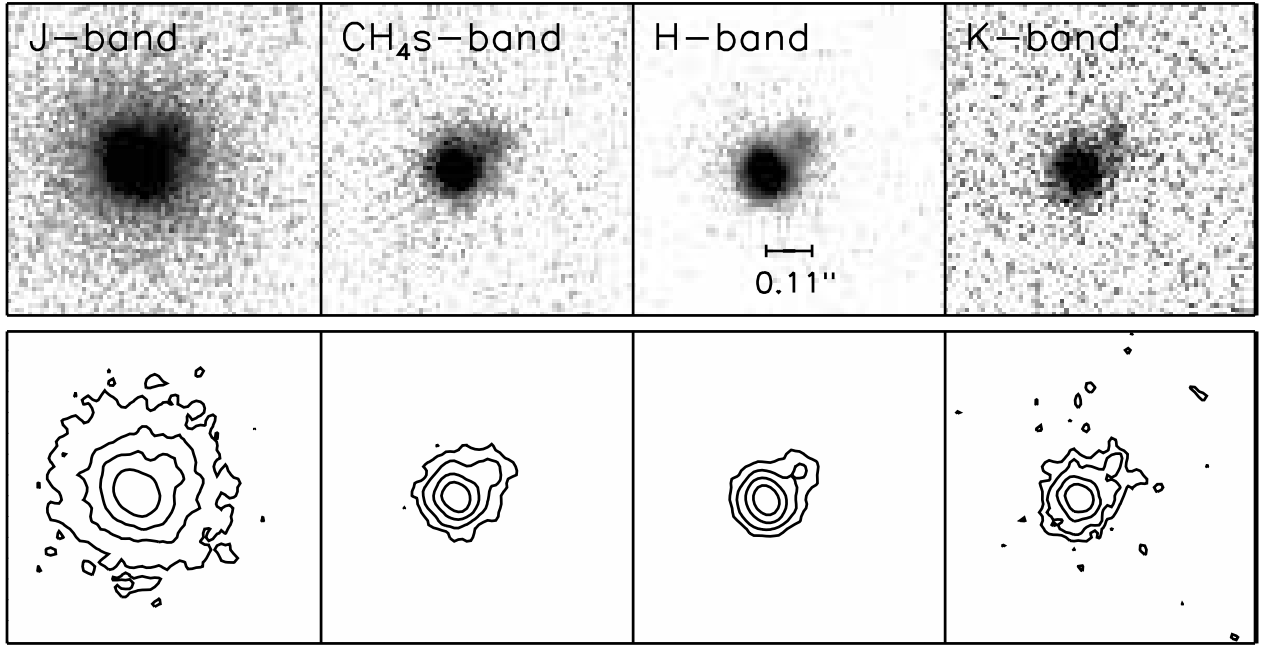


Fig. 1.— Keck LGS AO imaging of CFBDSIR J1458+1013AB. North is up and east is left. Each image is $0.75''$ on a side. The greyscale images are shown with a power-law stretch with an exponent of $1/4$. The contours are shown after smoothing the images by a 2-pixel gaussian. Contours are drawn from 90%, 45%, 22.5%, 11.2%, and 5.6% of the peak value in each bandpass.

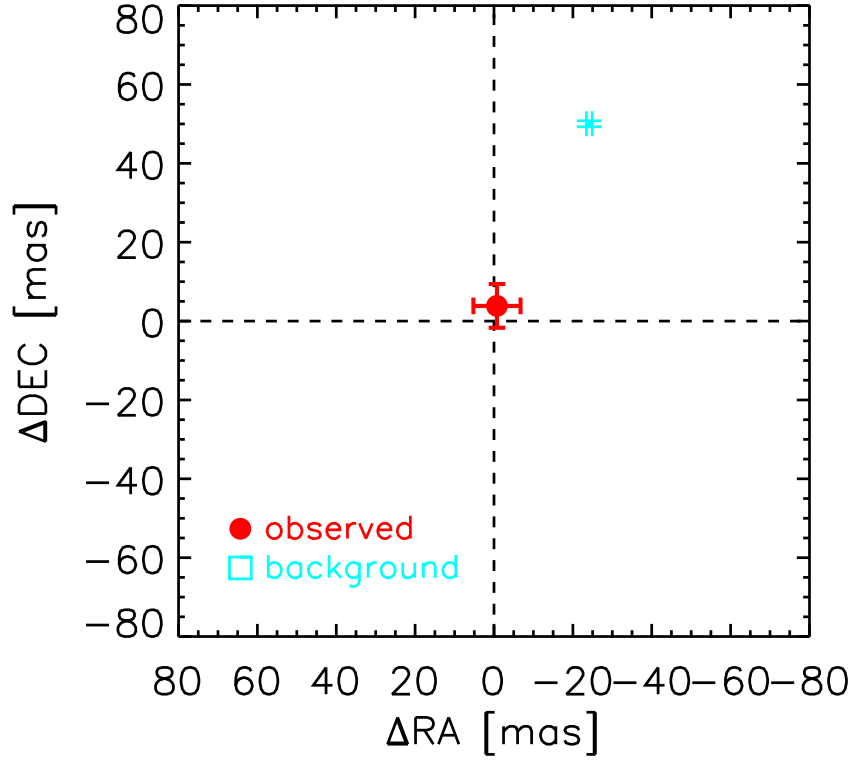


Fig. 2.— The change in the position of CFBDSIR J1458+1013B relative to CFBDSIR J1458+1013A. The red point shows the measured change from our two Keck LGS epochs, which is consistent with no motion. The blue symbol shows the expected motion (and its uncertainties) if component B is a background source, given the measured parallax and proper motion of CFBDSIR J1458+1013. (Over the 1.5 month time baseline between Keck epochs, the proper motion dominates.) The two points are inconsistent at 9.1σ , indicating that the system is a physical binary.

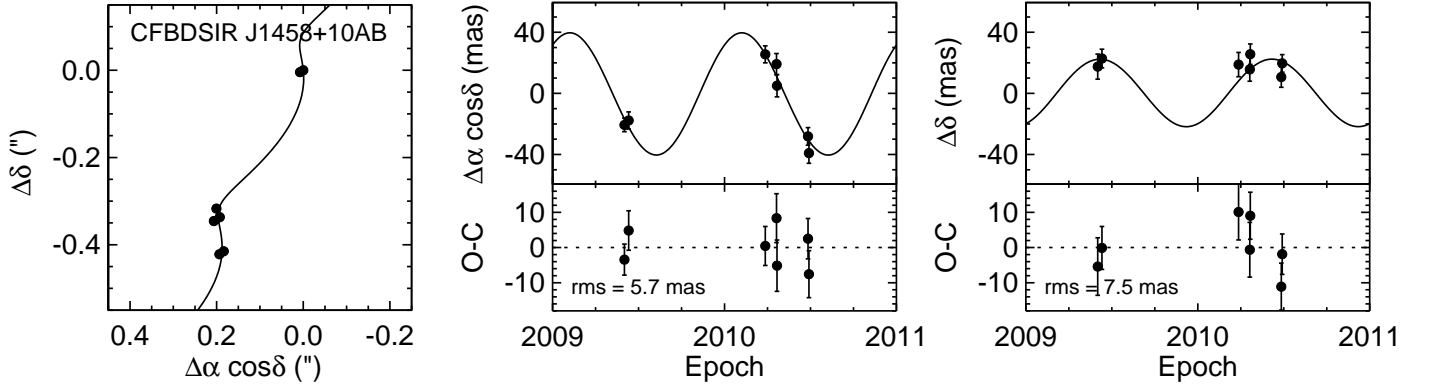


Fig. 3.— *Left:* Relative astrometry from CFHT/WIRCam J -band imaging of CFBDSIR J1458+1013AB that shows both proper motion and parallax. The origin corresponds to the first epoch of data. *Middle and Right:* Top panels show relative astrometry in α and δ , respectively, as a function of Julian year after subtracting the best-fit proper motion. (This is for display purposes only; in our analysis we fit for both proper motion and parallax simultaneously.) Bottom panels show the residuals after subtracting both parallax and proper motion.

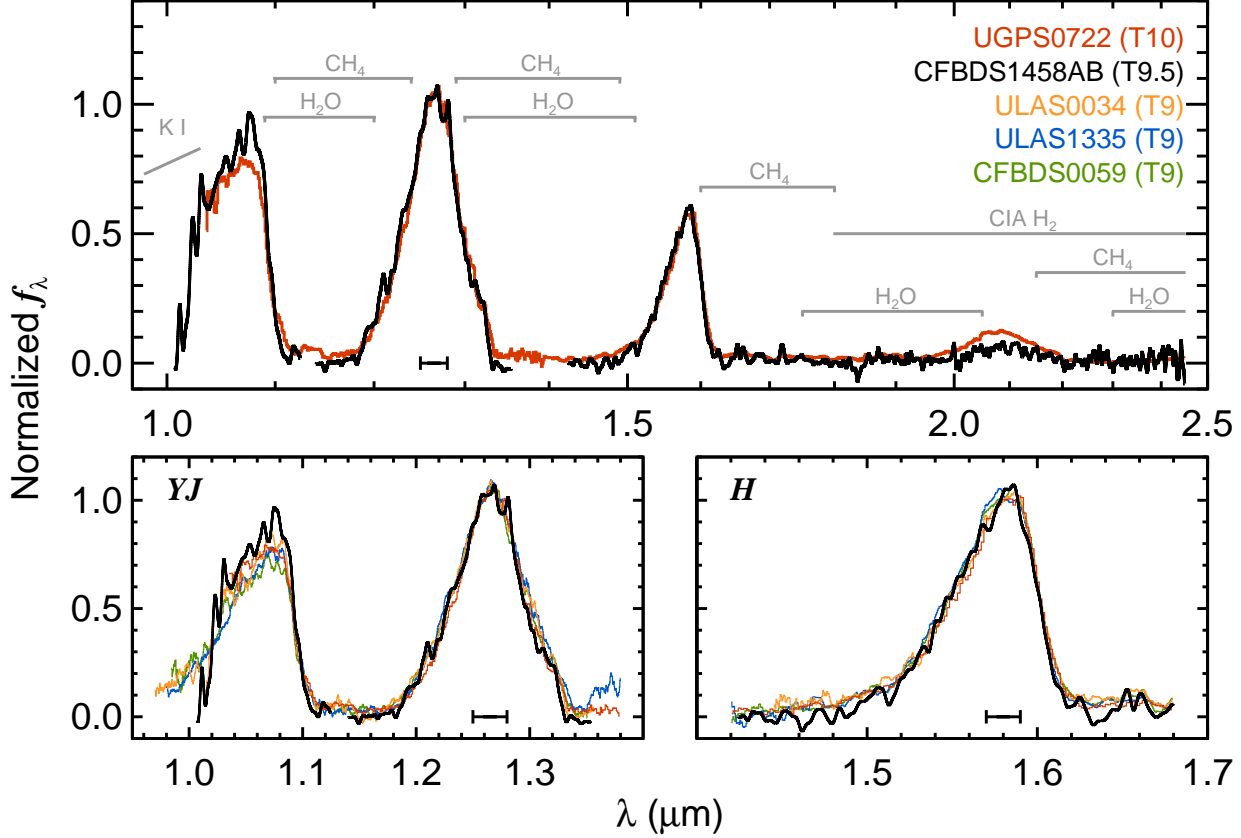


Fig. 4.— The integrated-light near-IR spectrum of CFBDSIR J1458+1013AB (black line) compared with other late-T dwarfs. The spectra have been smoothed for clarity. The upper panel shows a comparison with the T10 dwarf UGPS J0722–05 (red line; Lucas et al. 2010). The lower panels show the *YJ* (left) and *H*-band (right) comparison with UGPS J0722–05 and three T9 dwarfs (Warren et al. 2007; Burningham et al. 2008; Delorme et al. 2008a). The black horizontal bars near the bottom of the plots show the wavelength ranges used to normalize the spectra (1.25–1.28 μm for the top and bottom left plots, and 1.57–1.59 μm for the bottom right plot). Note that for the upper panel, the x-axis uses a log scale to help make the bluer bandpasses more visible.

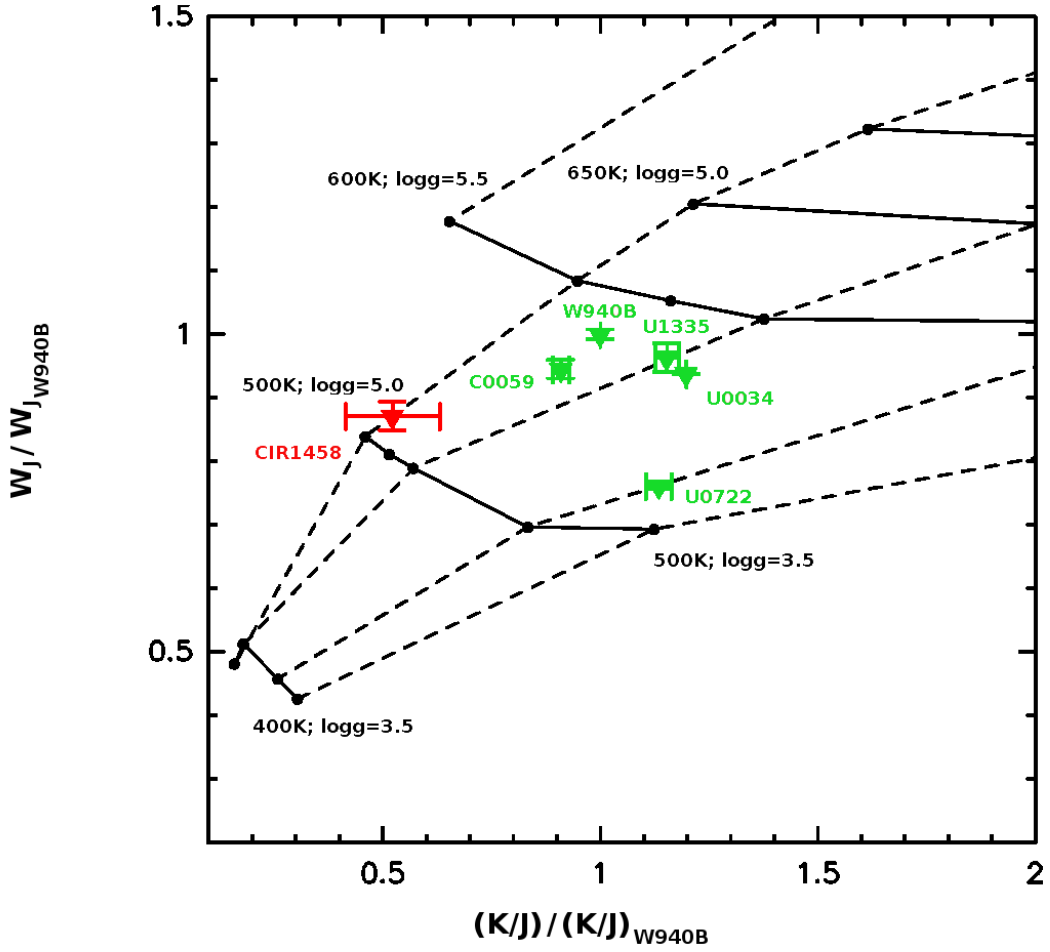


Fig. 5.— The W_J and J/K spectral indices for very late-T dwarfs compared to the solar-metallicity BT-Settl-2009 model atmospheres. (See Table 4 for measurements and references.) The model grid has been scaled to agree with the T8.5 benchmark dwarf Wolf 940B ($T_{\text{eff}} = 575$ K, $\log(g) = 4.75$; Burningham et al. 2009). The plotted errors represent the 1σ uncertainties in the index measurements.

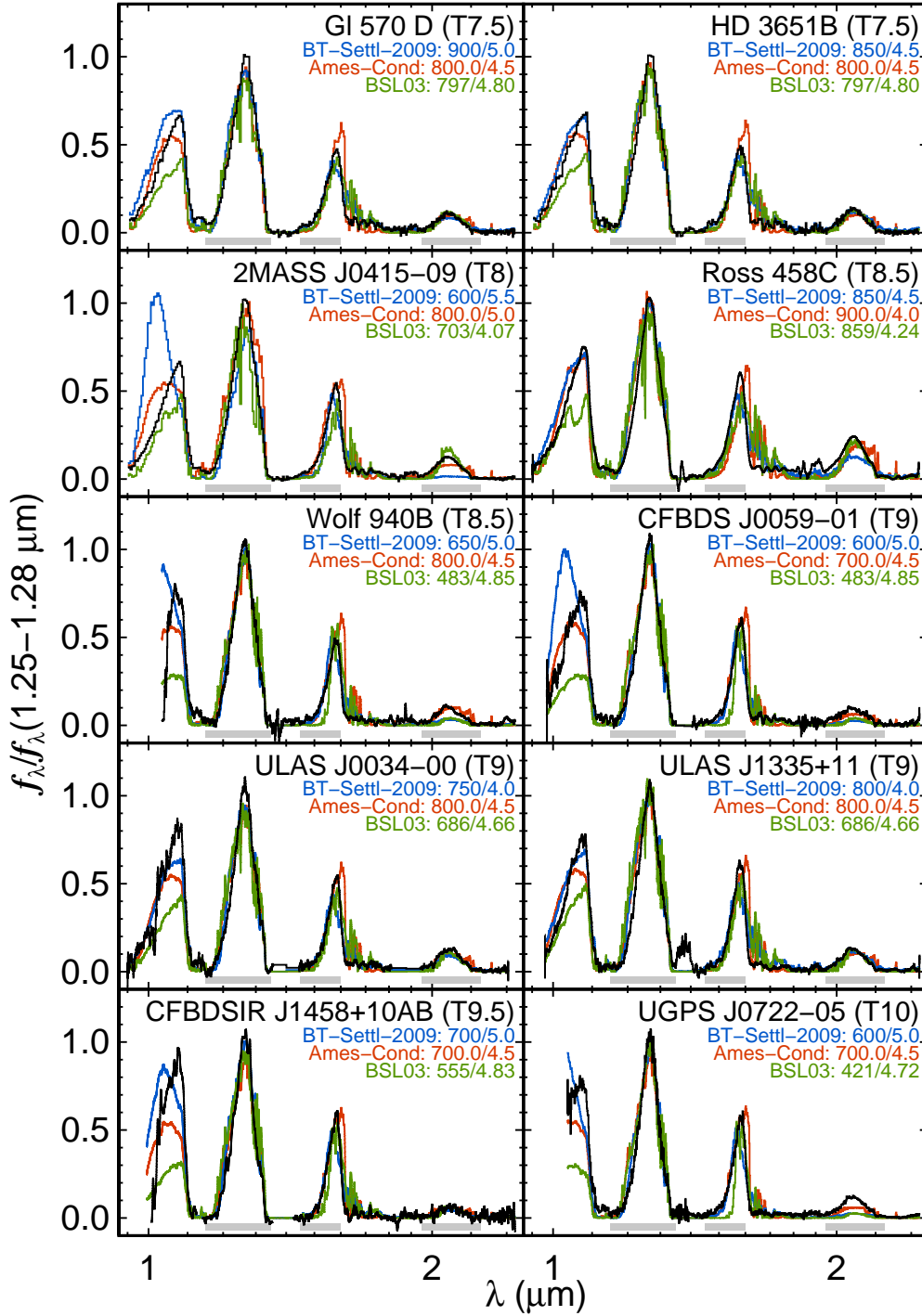


Fig. 6.— Best-fitting BT-Settl-2009 (blue), Ames-Cond (red), and BSL03 (green) model atmospheres to late-T dwarfs with parallaxes. (See also Table 5.) The gray horizontal bars show the wavelengths used in the fit, chosen to avoid known systematic errors in the models (e.g., the Y -band and the red side of the H -band) and regions of low S/N. The observed spectra are normalized to unity flux between 1.25–1.28 μm , and the normalization of the models is an outcome of the fitting process. The observed spectra for Ross 458C, Wolf 940B, CFBDS J0059–01, ULAS J0034–00, and ULAS J1335+11 are smoothed for clarity here, but the models were fit to the original (unsmoothed) data. Note that the x-axis uses a log scale, to help make the bluer bandpasses more visible.

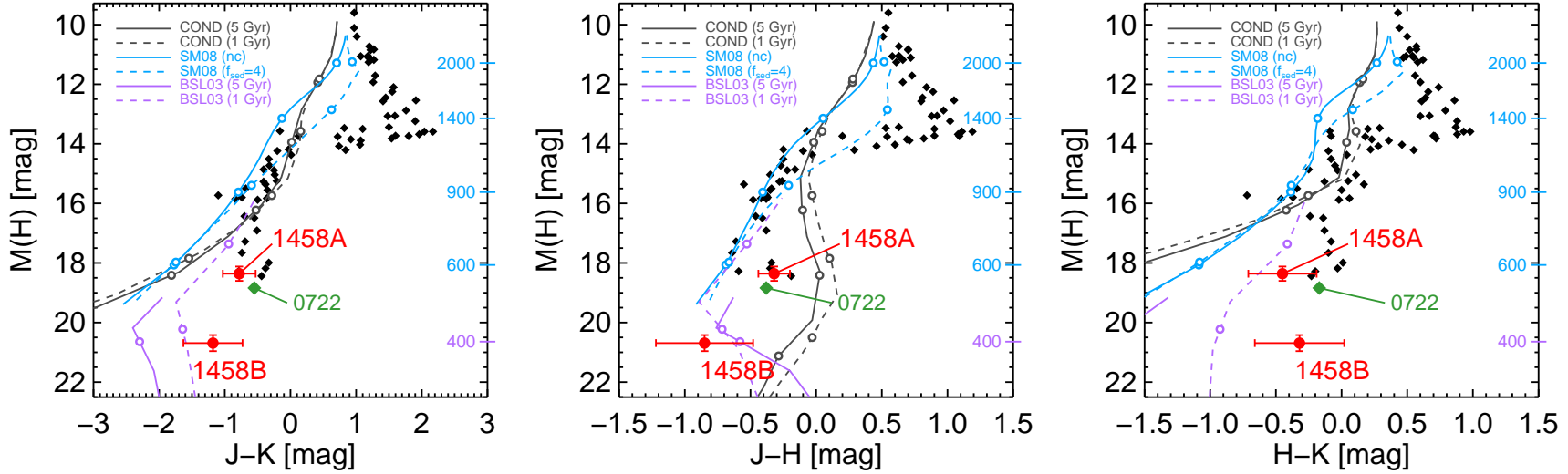


Fig. 7.— Color-magnitude diagrams comparing CFBDSIR J1458+1013AB (red dots) to field L and T dwarfs with parallaxes (Dahn et al. 2002; Tinney et al. 2003; Vrba et al. 2004; Marocco et al. 2010), based on the compilation by Leggett et al. (2010b) and plotted as filled diamonds. Known binaries are excluded. The T10 dwarf UGPS J0722–05 is labeled. We also show the Lyon/COND (Baraffe et al. 2003), Saumon & Marley (2008), and Burrows et al. (2003) models. For the SM08 models, we plot the $\log(g) = 5$ models that have a moderate cloud layer ($f_{sed} = 4$) and those that have no clouds (“nc”). The open circles on the model tracks demarcate a common set of T_{eff} ’s; for models plotted with a solid line, the corresponding T_{eff} values are listed on the right hand axis for the Saumon & Marley models (which go down to 500 K) and then the BSL03 models for cooler temperatures. This combination is chosen for the labels because it agrees better with the data than the Lyon/COND models, though in general no single model agrees well with the loci of the latest T dwarfs and CFBDSIR J1458+1013B.

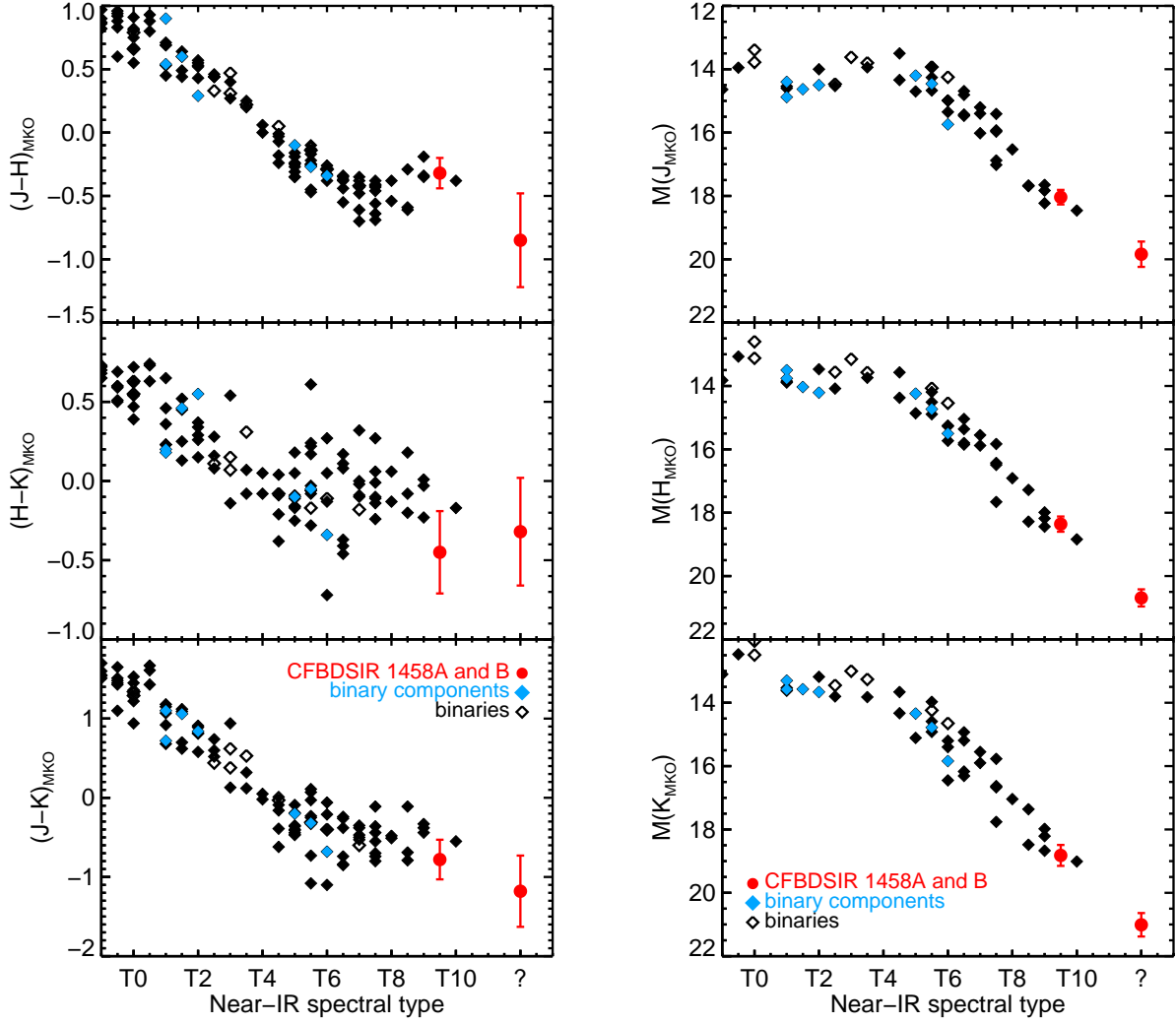


Fig. 8.— Comparison of the colors and magnitudes of CFBDSIR J1458+1013A and B to those of field objects. The latter come from the compilation of Leggett et al. (2010b), augmented with resolved photometry of tight ultracool binaries (McCaughrean et al. 2004; Liu & Leggett 2005; Liu et al. 2006).

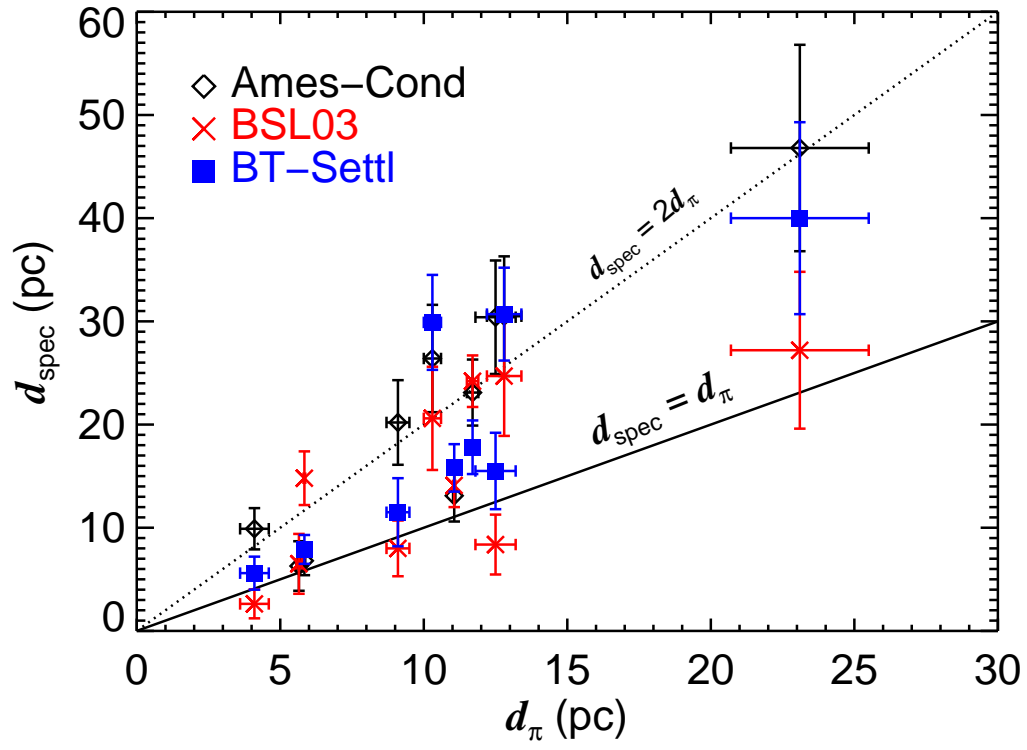


Fig. 9.— Comparison of model-derived spectroscopic distances (d_{spec}) using the method of Bowler et al. (2009) with the parallax distances (d_{π}) for the sample of late-T dwarfs in Table 5. See Appendix for details.

Table 1. Keck LGS AO Observations

Date (UT)	Filter ^a	Airmass	FWHM (mas)	Separation (mas)	Position angle (deg)	Δmag
2010-May-22	CH_4s	1.14	62 ± 6	108 ± 6	308 ± 2	2.17 ± 0.12
2010-Jul-08	J	1.33	94 ± 10	110 ± 11	308 ± 4	1.8 ± 0.4
	H	1.04	61 ± 4	111 ± 3	309.3 ± 1.4	2.33 ± 0.14
	K	1.11	60 ± 3	122 ± 6	314 ± 2	2.2 ± 0.2

Note. — All photometry on the MKO system. The tabulated uncertainties on the imaging performance (FWHM and Strehl ratio) are the RMS of the measurements from the individual images.

Table 2. CFHT/WIRCAM *J*-band Astrometry of CFBDSIR J1458+1013

N_{ep}	N_{ref}	Epoch 1	Δt (yr)	ΔAM	$N_{\text{fr}}(N_{\text{cal}})$	μ (mas/yr)	P.A. ($^{\circ}$)	π_{rel} (mas)	$\Delta \pi$ (mas)	π_{abs} (mas)	χ^2 (dof)
7	72	2009.42	1.07	0.03	68 (8)	432 ± 6	154.2 ± 0.7	42.4 ± 4.5	0.9 ± 0.1	43.3 ± 4.5	11.5 (9)

Note. — N_{ep} = Number of distinct observing epochs (i.e., nights); N_{ref} = Number of reference stars used; Epoch 1 = Date of our first WIRCam observation; Δt = Time baseline for the observations; ΔAM = Maximum difference in airmass over all epochs; N_{fr} = Total number of frames obtained (10–11 per epoch); N_{cal} = Subset of reference stars used in the absolute calibration; $\Delta \pi$ = Correction applied to the best-fit parallax to determine the absolute parallax ($\pi_{\text{abs}} = \pi_{\text{rel}} + \Delta \pi$).

Table 3. Properties of CFBDSIR J1458+1013AB

Property	Component A	Component B
Integrated-light spectral type		T9.5
d (pc)		23.1 ± 2.4
Projected separation (AU)		2.6 ± 0.3
v_{tan} (km/s)		47 ± 5
J (mag)	19.86 ± 0.07	21.66 ± 0.34
CH_4s (mag)	19.73 ± 0.10	21.90 ± 0.15
H (mag)	20.18 ± 0.10	22.51 ± 0.16
K (mag)	20.63 ± 0.24	22.83 ± 0.30
$J - H$ (mag)	-0.32 ± 0.12	-0.85 ± 0.37
$J - K$ (mag)	-0.78 ± 0.25	-1.18 ± 0.45
$CH_4s - H$ (mag)	-0.45 ± 0.14	-0.61 ± 0.22
$H - K$ (mag)	-0.45 ± 0.26	-0.32 ± 0.34
$M(J)$ (mag)	18.04 ± 0.23	19.84 ± 0.40
$M(CH_4s)$ (mag)	17.91 ± 0.24	20.08 ± 0.27
$M(H)$ (mag)	18.36 ± 0.24	20.69 ± 0.27
$M(K)$ (mag)	18.82 ± 0.33	21.02 ± 0.37
Near-IR spectral type	T9.5	>T10
$\log(L_{bol}/L_{\odot})$ (dex)	-6.02 ± 0.14	-6.74 ± 0.19
Evolutionary model results for 1.0 and 5.0 Gyr: Lyon/COND models and L_{bol}		
Mass (M_{Jup})	$12.1 \pm 1.9, 31 \pm 4$	$5.8 \pm 1.3, 14 \pm 3$
Total mass (M_{Jup})		$18 \pm 2, 45 \pm 5$
q ($\equiv M_B/M_A$)		$0.48 \pm 0.14, 0.45 \pm 0.12$
$T_{eff}(K)$	$556 \pm 48, 605 \pm 55$	$360 \pm 40, 380 \pm 50$
$\log(g)$ (cgs)	$4.45 \pm 0.07, 5.00 \pm 0.08$	$4.10 \pm 0.10, 4.58 \pm 0.11$
Orbital period (yr)		$35^{+28}_{-10}, 22^{+18}_{-6}$
Evolutionary model results for 1.0 and 5.0 Gyr: Burrows et al. (1997) models and L_{bol}		
Mass (M_{Jup})	$13 \pm 2, 36 \pm 4$	$6.8 \pm 1.5, 17 \pm 4$
Total mass (M_{Jup})		$20 \pm 3, 53 \pm 6$
q ($\equiv M_B/M_A$)		$0.53 \pm 0.15, 0.47 \pm 0.13$
$T_{eff}(K)$	$550 \pm 50, 600 \pm 60$	$350 \pm 40, 380 \pm 50$
$\log(g)$ (cgs)	$4.47 \pm 0.07, 5.06 \pm 0.07$	$4.14 \pm 0.10, 4.65 \pm 0.12$
Orbital period (yr)		$33^{+27}_{-9}, 20^{+17}_{-6}$
Evolutionary model results for 1.0 and 5.0 Gyr: Burrows et al. (2003) models and $M(J)$		
Mass (M_{Jup})	$11.1 \pm 0.7, >25$	$7.6 \pm 0.6, 18.8 \pm 1.3$
Total mass (M_{Jup})		$18.7 \pm 0.9, >44$
q ($\equiv M_B/M_A$)		$0.68 \pm 0.07, <0.75$
$T_{eff}(K)$	$479 \pm 20, >483$	$386 \pm 15, 407 \pm 15$
$\log(g)$ (cgs)	$4.37 \pm 0.03, >4.85$	$4.19 \pm 0.04, 4.69 \pm 0.03$
Orbital period (yr)		$34^{+28}_{-10}, <22$

Note. — All infrared photometry on the MKO photometric system. For the 5 Gyr Burrows et al. (2003) evolutionary model fits, component A is brighter in $M(J)$ than the model grid, so its derived physical parameters are listed as limits.

Table 4. Spectral indices for very late-T dwarfs.

Object	Sp. Type	H ₂ O-J	W _J	CH ₄ -J	H ₂ O-H	CH ₄ -H	NH ₃ -H	CH ₄ -K	K/J
Wolf 940B	T8.5	0.030 ± 0.005	0.274 ± 0.002	0.1521 ± 0.0009	0.142 ± 0.002	0.090 ± 0.002	0.537 ± 0.002	0.072 ± 0.013	0.1113 ± 0.0014
ULAS J0034−00	T8.5	0.012 ± 0.006	0.262 ± 0.004	0.145 ± 0.009	0.133 ± 0.010	0.097 ± 0.006	0.510 ± 0.011	0.092 ± 0.015	0.128 ± 0.003
CFBDS J0059−01	T8.5	0.029 ± 0.005	0.257 ± 0.004	0.165 ± 0.005	0.119 ± 0.008	0.084 ± 0.002	0.526 ± 0.005	0.128 ± 0.037	0.101 ± 0.002
CFBDSIR J1458+1013AB	T9.5	−0.002 ± 0.008	0.237 ± 0.006	0.103 ± 0.009	0.078 ± 0.016	0.044 ± 0.018	0.54 ± 0.02	0.06 ± 0.19	0.058 ± 0.012
UGPS J0722−05	T10	0.0339 ± 0.0017	0.2074 ± 0.0012	0.1358 ± 0.0019	0.1218 ± 0.0017	0.0643 ± 0.0013	0.492 ± 0.002	0.096 ± 0.002	0.1262 ± 0.0003

Note. — Near-IR spectral indices and provisional spectral types for some of the latest-type brown dwarfs (Warren et al. 2007; Burningham et al. 2009; Delorme et al. 2008a; Lucas et al. 2010). The index definitions are from Burgasser et al. (2006b), Warren et al. (2007), and Delorme et al. (2008a). Note that the negative value of H₂O-J for CFBDSIR J1458+1013 is due to the fact that there is no detected flux in the 1.14–1.165 μ m water absorption band probed by this index.

Table 5. Atmospheric Model Fits to Late-T Dwarfs with Parallaxes

Name	Ref	Ames-Cond					BSL03					BT-Settl-2009					d_π (σ_π) (pc)	π Ref
		T_{eff} (K)	$\log g$ (cgs)	R^a (R_{Jup})	d_{spec} (pc)	$(\sigma_{\text{mc}}, \sigma_{\text{tot}})^b$ (pc)	T_{eff} (K)	$\log g$ (cgs)	R^c (R_{Jup})	d_{spec} (pc)	$(\sigma_{\text{mc}}, \sigma_{\text{tot}})^b$ (pc)	T_{eff} (K)	$\log g$ (cgs)	R^c (R_{Jup})	d_{spec} (pc)	$(\sigma_{\text{mc}}, \sigma_{\text{tot}})^b$ (pc)		
Gl 570D (T7.5)	1	800	4.5	1.06	6.8	(0.1, 1.4)	797 ^d	4.80 ^d	0.996	14.8	(0.2, 2.6)	900	5.0	0.903	7.9	(0.2, 1.4)	5.84 (0.03) ^e	13
HD 3651B (T7.5)	2, 3	800	4.5	1.06	13.1	(0.2, 2.5)	797 ^d	4.80 ^d	0.996	14.1	(0.2, 2.1)	850	4.5	1.07	15.8	(0.2, 2.3)	11.06 (0.04)	13
2MASS J0415−09 (T8)	4	800	5.0	0.89	6.29	(0.09, 2.4)	703	4.07	1.33	6.50	(0.1, 2.9)	600	5.5	... ^f	... ^f	5.65 (0.09)	14	
Ross 458C (T8.5)	5, 6	900	4.0	1.24	23.1	(0.09, 3.2)	859 ^d	4.24 ^d	1.27	24.2	(0.1, 2.5)	850	4.5	1.07	17.8	(0.1, 2.6)	11.7 (0.2)	13
Wolf 940B (T8.5)	7	800	4.5	1.06	30.4	(0.3, 5.5)	483 ^d	4.85 ^d	0.924	8.37	(0.07, 2.9)	650	5.0	0.874	15.5	(0.1, 3.7)	12.5 (0.7)	15
CFBDS J0059−01 (T9)	8	700	4.5	1.04	20.2	(0.3, 4.1)	483 ^d	4.85 ^d	0.924	8.01	(0.1, 2.7)	600	5.0	0.879	11.5	(0.2, 3.3)	9.2 (0.4)	16
ULAS J0034−00 (T9)	9	800	4.5	1.06	30.5	(0.5, 5.8)	686	4.66	1.04	24.7	(0.4, 5.8)	750 ^d	4.0 ^d	1.17	30.7	(0.5, 4.5)	12.8 (0.6)	16, 17
ULAS J1335+11 (T9)	10	800	4.5	1.06	26.4	(0.2, 5.2)	686	4.66	1.04	20.6	(0.1, 5.0)	800 ^d	4.0 ^d	1.21	29.9	(0.1, 4.6)	10.3 (0.3)	16
CFBDSIR J1458+1013AB (T9.5) ^g	11	700	4.5	1.04	46.8	(1.0, 10)	555 ^d	4.83 ^d	0.946	27.2	(0.9, 7.6)	700	5.0	0.880	40.0	(0.8, 9.3)	23.1 (2.4)	18
UGPS J0722−05 (T10)	12	700	4.5	1.04	9.9	(0.1, 2.0)	421 ^d	4.72 ^d	0.961	2.62	(0.02, 1.4)	600	5.0	0.879	5.6	(0.1, 1.6)	4.1 (0.5)	12

Note. — Best-fitting Ames-Cond (Allard et al. 2001), BSL03 (Burrows et al. 2003), and BT-Settl-2009 (Allard & Freytag 2010) model spectra to the combined 1.15–1.35 μm , 1.45–1.6 μm , and 1.95–2.25 μm regions of the observed spectra.

^aRadius derived from an interpolated grid of Lyon/Cond evolutionary models. This value corresponds to the best-fitting T_{eff} and $\log g$ Ames-Cond atmospheric model.

^bModel-derived spectroscopic distance estimate based on the method of Bowler et al. (2009). σ_{mc} denotes the Monte Carlo-derived distance error associated with the best-fitting atmospheric model and incorporates measurement and flux-calibration errors. σ_{tot} is the Monte Carlo-derived total measurement error in the distance, based on the measurement errors and assuming 1σ uncertainties of 50 K and 0.25 dex in T_{eff} and $\log g$ in the model atmosphere fits.

^cRadius computed using the best-fitting T_{eff} and $\log g$ and the power law fit to $R(T_{\text{eff}}, \log g)$ from Equation 1 of Burrows et al. (2003).

^dBest-fit model is at the edge of the model grid.

^eDistance to the primary Gl 570 A.

^fThe best-fitting model atmosphere parameters are outside the grid of evolutionary models, so there is no corresponding radius or distance estimate.

^gIntegrated light spectrum.

References. — 1–Burgasser et al. (2000); 2–Mugrauer et al. (2006); 3–Luhman et al. (2007); 4–Burgasser et al. (2002); 5–Goldman et al. (2010); 6–Scholz (2010b); 7–Burningham et al. (2009); 8–Delorme et al. (2008a); 9–Warren et al. (2007); 10–Burningham et al. (2008); 11–Delorme et al. (2010); 12–Lucas et al. (2010); 13–van Leeuwen (2007); 14–Vrba et al. (2004) 15–Harrington & Dahn (1980) 16–Marocco et al. (2010); 17–Smart et al. (2010); 18–this work.

Table 6. Physical Properties Derived from Model Atmospheres and Parallactic Distances

Name	Ames-Cond			BSL03			B'T-Settl-2009		
	T_{eff} (K)	$\log g$ (cgs)	M (M_{Jup})	T_{eff} (K)	$\log g$ (cgs)	M (M_{Jup})	T_{eff} (K)	$\log g$ (cgs)	M (M_{Jup})
Gl 570D (T7.5)	780–880	4.7–5.4	21–54	>520	>4.4	>13	760–880	4.7–5.4	21–54
HD 3651B (T7.5)	780–880	4.7–5.4	21–54	>700	>4.6	>22	740–860	4.7–5.4	20–54
2MASS J0415–09 (T8)	790–800	4.7–5.3	23–53	>660	>4.6	>19	600–720	4.5–5.2	9–45
Ross 458C (T8.5)	690–760	4.0–4.7	6–20	>590	>3.9	>5	660–740	4.0–4.7	6–20
Wolf 940B (T8.5)	570–680	4.5–5.2	12–43	>500	>4.4	>12	560–640	4.4–5.2	12–42
CFBDS J0059–01 (T9)	520–600	4.4–5.2	10–35	>440	>4.3	>10	500–600	4.4–5.1	11–34
ULAS J0034–00 (T9)	560–680	4.5–5.2	12–43	>500	>4.4	>12	560–660	4.4–5.2	12–42
ULAS J1335+11 (T9)	560–660	4.4–5.2	12–42	>500	>4.4	>12	560–640	4.4–5.2	12–42
CFBDSIR J1458+1013AB (T9.5) ^a	520–640	4.4–5.2	11–42	>460	>4.3	>10	520–620	4.4–5.2	11–36
UGPS J0722–05 (T10)	480–600	4.4–5.1	10–35	>420	>4.3	>9	480–580	4.4–5.1	10–33

^aIntegrated light spectrum.